A multiscale framework for aero-thermo-chemical DFT/CFD simulation for re-entry environment

Jongkyung An[1], Seunghwan Kwon[1], Jiseon Ahn[1], Rajkamal Anand [1] , Gun Jin Yun [2]

Abstract

Ultra High-Temperature Ceramics (UHTC) are being developed as surface materials for re-entry vehicles in Low Earth Orbit (LEO) environments due to their resilience to the effects of atomic oxygen(AO). However, evaluating the performance of UHTC ceramic materials through experiments consumes a significant amount of time and resources. To address this, we have developed a DFT/CFD multiscale framework for the re-entry performance assessment of heat shield materials. firstly , verification was conducted for the use of DFT properties as input parameters for CFD analysis by comparing DFT properties and experimental data. Secondly, the investigation explored high-temperature oxidation mechanisms of UHTCs on different surface orienataitons, employing Ab initio Molecular Dynamics (AIMD) , Density Functional Theory(DFT) simulations This enabled us to perform space environment CFD simulations using DFT properties and obtatined a multiscale understanding of the oxidation performance of re-entry bodies with heat shielding materials.

Keywords : re-entry, multiscale simulation, DFT(density functional theory), CFD(Computational fluid dynamics), UHTC(Ultra High-Temperature Ceramics), AIMD(Ab initio molecular dynamics), High-Temperature

1. Introduction

The re-entry environment is chemically complex and exposed to high temperatures, typically including the Low Earth Orbit (LEO) region. One of the hazards in LEO is atomic oxygen (AO) bombardment, which damages surfaces [1]. To withstand such extreme conditions, heat shield materials are used, and the promising candidate for this purpose is Ultra High-Temperature Ceramics (UHTCs). Zirconium carbide (ZrC) , Hafnium carbide(HfC) is a well-known UHTC material with high melting temperature, low density, and high thermal and electric conductivity. Carbide materials are adversely affected by oxidation when exposed to specific environments, notably the leading edges of spacecraft during atmospheric re-entry, where temperatures exceed 2000°C in an oxidizing atmosphere. To assess the suitability of UHTCs in a such high temperature re-entry environment, investigation of temperature-dependent oxidation behavior,mechanical and thermal properties is essential [2]. Density functional theory (DFT) calculation can accelerate the efficiency of gaining such materials properties by reducing the time and cost required for experiments.

It can effectively reduce time cost, which is indispensable for understanding oxidation which is domain hazrd at space environment, and will accelerate Computational Fluid Dynamics (CFD) analysis [3] that simulates space conditions is essential to evaluate performance directly in re-entry environments. Several key input parameters (density, heat-capacity, thermal conductivity, thermal expansion coefficient…) are required for such CFD analysis. In this study, we have developed a more effective performance evaluation method by obtaining these input propertiess through Density Functional Theory (DFT) calculations, reducing the time cost for obtaining properties that can only be obtained through

[1] *Aerospace Engineering Department, Seoul National University, 1, Gwanak-ro, Gwanak-gu, Seoul, Republic of Korea, ajk7419@snu.ac.kr*
[1] *Aerospace Engineering Department, Seoul National University, 1, Gwanak-ro, Gwanak-gu, Seoul, Republic of Korea, sh.kwon@snu.ac.kr*
[1] *Aerospace Engineering Department, Seoul National University, 1, Gwanak-ro, Gwanak-gu, Seoul, Republic of Korea, jsahn00@snu.ac.kr*
[1] *Aerospace Engineering Department, Seoul National University, 1, Gwanak-ro, Gwanak-gu, Seoul, Republic of Korea, rajkamal35@snu.ac.kr*
[2] *Aerospace Engineering Department, Seoul National University, 1, Gwanak-ro, Gwanak-gu, Seoul, Republic of Korea, gunjin.yun@snu.ac.kr*

experiments. Through this method, we performed a CFD oxidation performance analysis using DFT properties and COMSOL default properties and compared the two performances..

After obtaining the oxidation performance at the continuum scale, we investigated the early stages of the oxidation process to understand this oxidation phenomenon at a smaller scale, which typically generates a porous oxide layer because of gaseous by-products (CO_2 and CO) escaping from the material, thereby increasing its permeability to oxygen. In this oxidation process of UHTCs encompasses various competing mechanisms, including the interaction of O, the formation of oxides, and the emission of CO and CO_2 as hot gases. This process leads to the development of porosity, thermal stresses, and residual stresses, which in turn cause microcracking, corner cracking, and spallation on the surface layer. Previous Research has highlighted the role of a complex array of factors on the oxidation kinetics of UHTCs, including their composition, the presence of additives, the method of manufacture, the microstructural characteristics, as well as the temperature, duration, and environmental oxygen partial pressure. To date, explicit and compelling evidence is absent regarding the initial formation of CO on the metal carbide (MC) surface, along with a lack of a comprehensive theoretical or experimental dynamic model of CO formation. To elucidate the eventual construction of the oxide layer, this research meticulously investigates the early stages of the oxide layer formation and extends these findings to predict the growth patterns of the oxide layer in subsequent stages. For describing oxidation behavior of UHTCs , physical properties(bonding information, charge density, adsorption energy, activation energy barriers, diffusion coeffcients) are caculated using DFT, AIMD, metadynamics (MetaD) simulation.

2. Methods

2.1. Thermal/Mechanical properties

In this study, thermal and mechanical properties of ZrC and HfC were calculated via quasi-harmonic approximation (QHA) with the aid of PHONOPY code. In the QHA calculation, Helmholtz free energy $\boldsymbol{F(V,T)}$ was acquired by adding vibrational ($\boldsymbol{F_{vib}(V,T)}$) and electronic free energy ($\boldsymbol{F_{el}(V,T)}$) to lattice energy at 0 K ($\boldsymbol{E_0(V)}$)

$$F(V,T) = E_0(V) + F_{vib}(V,T) + F_{el}(V,T) \tag{1}$$

as shown in Eq.(1). Thermodynamic properties obtained from QHA in this study included coefficient of thermal expansion (α_V),

$$\alpha_V = \frac{1}{V}\left(\frac{\partial V}{\partial T}\right)_P \tag{2}$$

which is defined as Eq.(2), and heat capacity at constant pressure (C_p). The relation between these properties is expressed as Eq.(3),

$$C_P - C_V = \alpha_V^2(\mathrm{T})B(T)T \tag{3}$$

where C_V is heat capacity at constant pressure, while $B(T)$ is bulk modulus.

For QHA calculation mentioned above, first-principles calculations are performed via PAW with PBE, which is one of the GGA, from VASP. Initially, geometry optimization was implemented. To obtain high accuracy results, the cutoff energy of plane-wave basis set was set to 500 eV, while k-points for Brillouin zone sampling was set to 25 x 25 x 25 for geometry optimization of conventional unit cell of ZrC, HfC. After such optimization, force constants were calculated by obtaining energies from each strained 2 x 2 x 2 supercells with 500 eV cutoff energy and 5 x 5 x 5 k-points. Then, thermal or mechanical properties were obtained up to 2500 K.

2.2. Computational fluid dynamics (CFD)

The CFD analysis program used in this study, COMSOL Multiphysics, is capable of FEM-based Multiphysics analysis. The simulation was performed under 2D laminar flow conditions, and the ZrC single material was analyzed. The far-field was sized to minimize interference with the external flow.

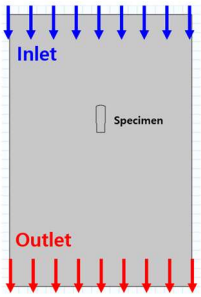

Figure 1. CFD Simulation Size

The specimen was a blunt body geometry, which was selected based on the most common specimen geometry. The analytical validation was performed at 1000K, 1500K, and 200K for laminar flow with default properties in COMSOL Multiphysics, and then compared to the values calculated at each temperature by substituting the thermal or mechanical properties obtained using DFT.

2.3. Interface Models

Table 1. Comparing the lattice parameters of *NaCl*-type TM monocarbides ZrC, and HfC, crystal structures with previously reported studies.

Systems	Lattice parameter 'a' (Å)			M-C bond length (Å)
	This work	DFT	Experiment	
ZrC	4.711	4.710[10–12]	4.69[10,13]	2.355
HfC	4.647	4.657[14]	4.634[15]	2.325
TaC	4.475	4.475[16]	4.456[13,15]	2.237

In this work, we considered a face-centred cubic crystal crystallised in a NaCl crystal structure space group of $Fm\bar{3}m$ type of the unit cells of metal carbides (MC) such as ZrC, HfC, and TaC were allowed to relax. Their lattice parameters were compared with those reported in previous studies (see **Table 1**).

Table 2. Comparing the lattice parameters ZrC, and HfC crystal structures of (100) and (111) surfaces.

Systems		Cell parameters				M-C bond length (Å)
		Lattice (Å)	Angles (deg)			
		a=b	α	β	γ	
100	ZrC	9.24	90	90	90	2.36
	HfC	9.29	90	90	90	2.33
111	ZrC	13.32	90	90	120	2.28
	HfC	13.14	90	90	120	2.23

To understand the oxidation mechanism of MCs, we modelled pristine MCs (100) and (111) surfaces from their corresponding bulk materials because it is the most stable. Supercells measuring 2 × 2 × 2 were constructed from the previously relaxed unit cells and cleaved for each surface orientation: (100) and (111) (see **Table 2**). Following the cleavage, a vacuum layer of 15 Å was introduced along the *z*-axis for each cleaved supercell. For the (111) surfaces, configurations with M-termination stacking were observed and displayed a significant rumpling with the M atoms displacing outward toward the vacuum while the C atoms relax inward. In contrast, for (100) surfaces, configurations featuring M and C-termination stacking were identified (the same number of carbon and metal atoms), and all system

information is displayed in **Figure 2**. In the model, four layers are constructed, with the bottom two layers fixed to simulate the bulk effect on the top two layers, which are allowed to relax freely.

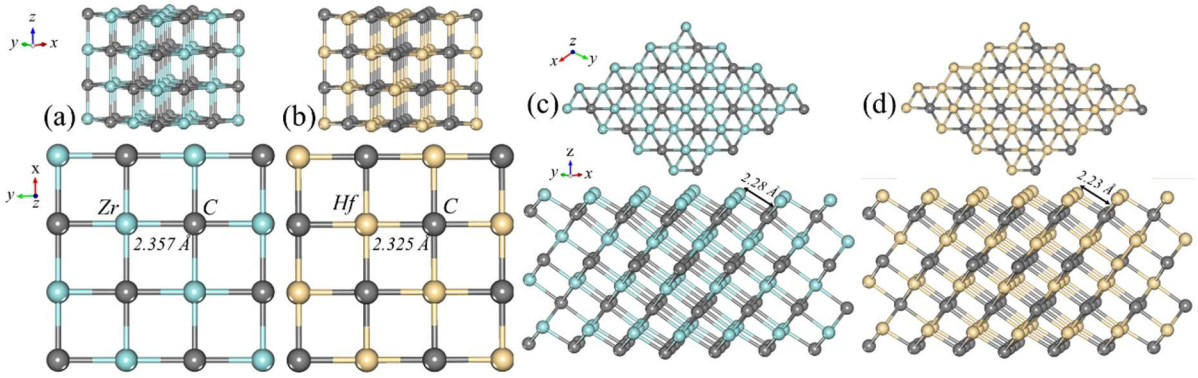

Figure 2. Optimized structures of MC (100) slab of side and top view of (a) ZrC, and (b) HfC

2.4. Calculation detatils

Vienna ab initio Simulation Package (VASP) was used for all DFT and AIMD calculations**.**

(a) Density Functional Theory (DFT)

All structures were optimized using the conjugate gradient algorithm. This optimization utilized the Perdew-Burke-Ernzerhof (PBE) exchange-correlation functional, a form of the generalized gradient approximation (GGA), in conjunction with the projector augmented-wave (PAW) method. The criteria for convergence were set at 0.01 eV/Å for ions and 10^{-6} eV for electrons. A cutoff energy of 500 eV and a *k*-mesh of 25 × 25 × 25 using the Monkhorst-Pack scheme were applied. Additionally, Gaussian smearing with a width of 0.03 eV was utilized in the simulations.

(b) AIMD - Calculation of diffusion coefficient

(c) Adsorption energy (ΔE)

For each configuration, ΔE per molecule is defined by

$$\Delta E = \left(E_{(ad\_O+surface)} - E_{(surface)} - E_{(\mu)} \right) \quad (4)$$

where $E_{(ad\_O+surface)}$ and $E_{(surface)}$ are the total energies of the MC surfaces with and without adsorbed O atom/s, respectively. $E_{(\mu)}$ represents the chemical potential of an isolated atom.

(d) Charge density difference (CDD)

To understand the nature of bonding between CAF molecule and carbon surface, CDD is calculated. It is defined as

$$\Delta\rho = \rho_{(Molecule+surf)} - \rho_{(surface)} - \rho_{(Molecule)} \quad (5)$$

where $\rho_{(Molecule+su)}$, $\rho_{(surface)}$ and $\rho_{(Molecule)}$, are total charge densities of CAF molecule adsorbed surface, bare surface, and isolated CAF molecule, respectively.

3. Results

3.1. Thermal/Mechanical properties

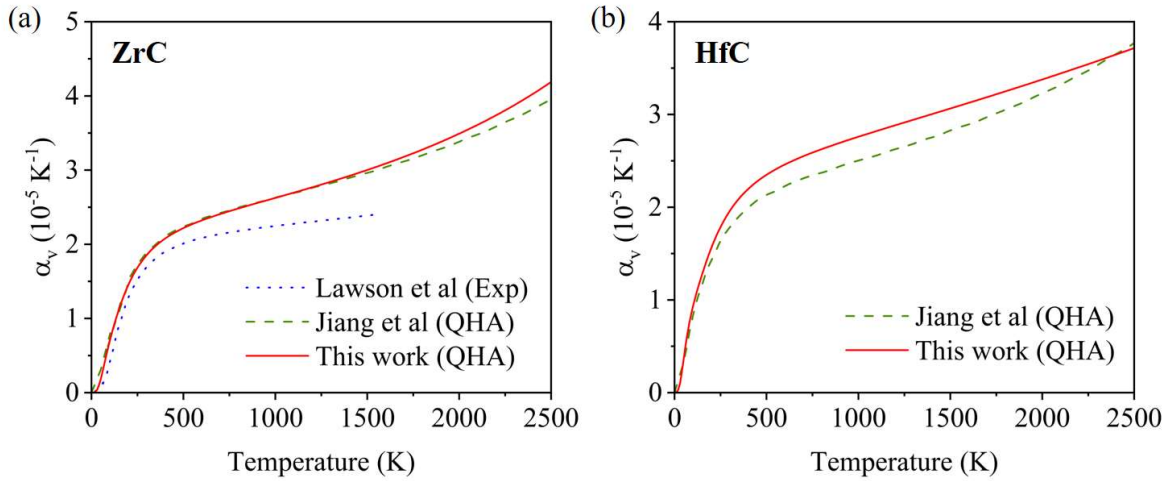

Figure 3. Coefficient of thermal expansion (α_V) along with temperature, calculated via quasi-harmonic approximation (QHA) in this work or from Jiang et al [17] and reported experimental values [18], of (a) ZrC and (b) HfC

According to **Figure 3**, graphs of calculated $\boldsymbol{\alpha_V}$, which is the vital parameter that determines the material resistance to thermal fluctuation, via QHA along with temperature are displayed. In the case of ZrC in **Figure 3**, previously reported QHA values were almost close to this work. Also, these values were closely matched to experimental values at lower temperature. However, these values were not matched to experimental results at higher temperature. Meanwhile, QHA results for previously reported work and this work were matched quite well, but there were not any experimental values available for HfC. It implies that QHA provides useful values when experimental reports are not available. In addition, $\boldsymbol{\alpha_V}$ was obviously higher for ZrC than HfC in **Figure 3**. This difference eventually determines the overall thermophysical properties of ZrC, HfC.

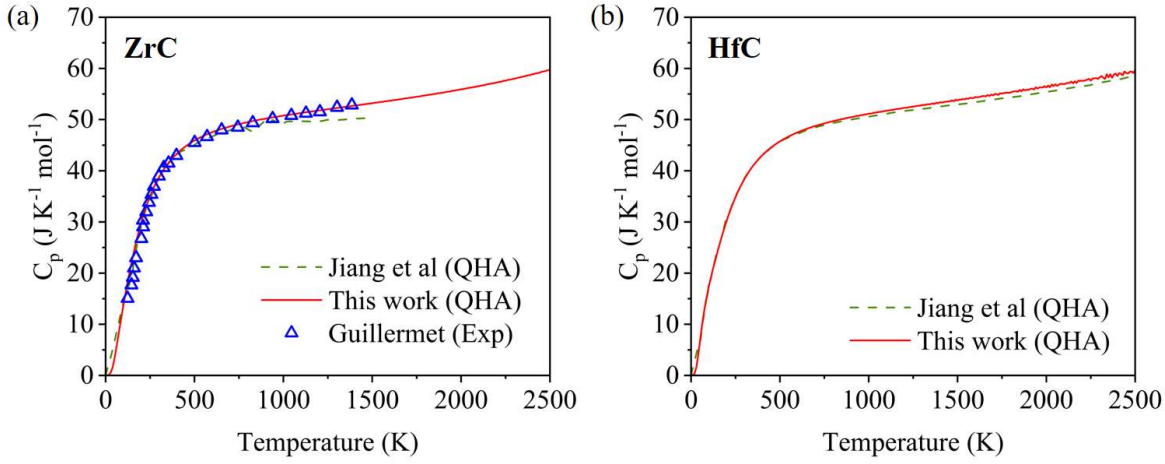

Figure 4. Heat capacity at constant pressure (C_p) along with temperature, calculated via QHA in this work or from Jiang et al [17] and reported experimental values [19], of (a) ZrC and (b) HfC

In **Figure 4**, the heat capacity at constant pressure ($\boldsymbol{C_p}$) results of ZrC, HfC are shown. Heat capacity is the essential property that can evaluate the thermal performance. According to **Figure4**, heat capacity increases steeply at lower temperature, while relatively slowly increases at higher temperature. It can be identified that $\boldsymbol{C_p}$ does not converge to Dulong-Petit limit unlike $\boldsymbol{C_V}$. Also, it is worth noting that $\boldsymbol{C_p}$ obtained from QHA in this work matched significantly similar to reported experimental values for ZrC. Moreover, as shown in Figure 2, $\boldsymbol{C_p}$ was slightly higher for ZrC when it is compared with HfC. Also, $\boldsymbol{C_p}$ of ZrC increased faster than HfC. Therefore, it can be deduced that HfC is more resistant to high temperature than ZrC.

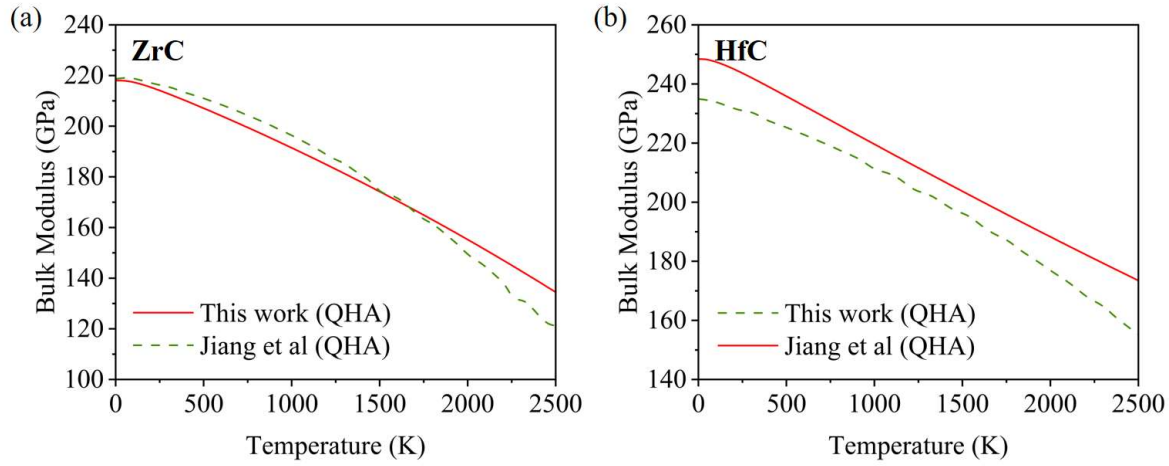

Figure 5. Bulk modulus along with temperature, calculated via QHA in this work or from Jiang et al [17], of (a) ZrC and (b) HfC

In **Figure 5**, bulk modulus of ZrC, HfC calculated from QHA in terms of temperature are plotted. This property is then compared with reported QHA results from Jiang et al [17] and it is in close agreement to values from this work. From this data, mechanical properties of material at finite temperature can be identified. As it is confirmed from **Figure 5**, bulk modulus consistently decreased with temperature increase. That is, mechanical properties will be degraded as temperature increases. Additionally, when compared between bulk modulus of ZrC and HfC in **Figure 5**, HfC clearly showed superior bulk modulus than ZrC. HfC possessed higher bulk modulus than ZrC at all temperature range. This fact implies that HfC has higher mechanical property even at high temperature, which is an essential property that makes it to be a good candidate for the usage on hypersonic environment.

3.2. CFD simulation

The basic calculations for the analytical validation were performed at 1000, 1500, and 2000 K with ZrC in 2D blunt body geometry. It can be seen that the surface concentration variation of ZrC increases with increasing temperature, as shown in **Figure 6**.

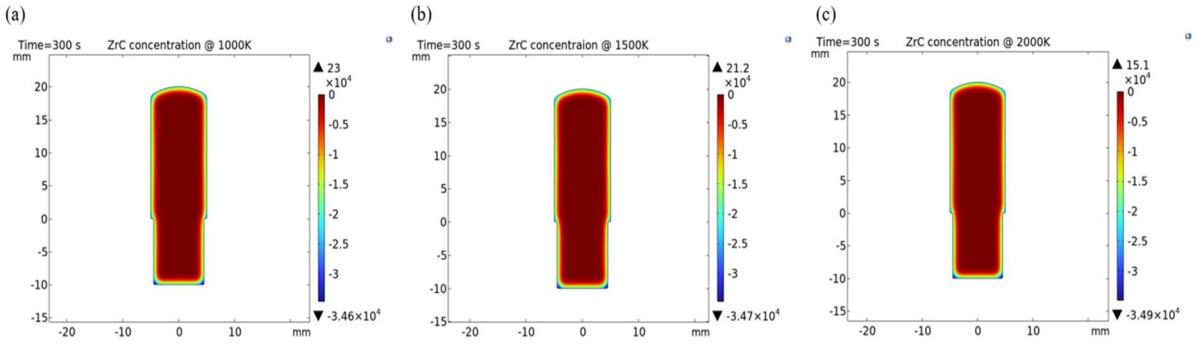

Figure 6. ZrC Concentration at each temperature

The cut-off point for judging ZrO_2 is when the concentration value of ZrC is -0.00015 mol/m^3 or less, and values below this threshold are judged to be the point at which the properties of ZrC change. This calculation is based on the part with a concentration of ZrC of 60% or less, which is assumed to be ZrO2. **Figure 7a** shows the percentage of ZrO_2 density normalized by replacing the concentration value with the density value, and as the temperature increases, the percentage value also tends to increase. In the case of overall density, the density of ZrO_2 relative to ZrC tends to increase as the temperature increasing, but when linear ablaiton rate as shown in **Figure 7b**, it is confirmed that the ZrO_2 oxide layer becomes thinner as the temperature increases. Linear ablation rate is Eq. (6),
the oxidation layer thickness divided by the total analysis time.

This is likely due to the fact that the CFD calculation recognizes all non-ZrC as ZrO2, and therefore interprets the range of ZrO_2 to include gaseous substances such as CO and CO_2 that are vaporized. Therefore, future work will aim to accurately measure the thickness of the oxide layer.

$$\mathrm{LAR} = \frac{d_i - d_t}{t} \tag{6}$$

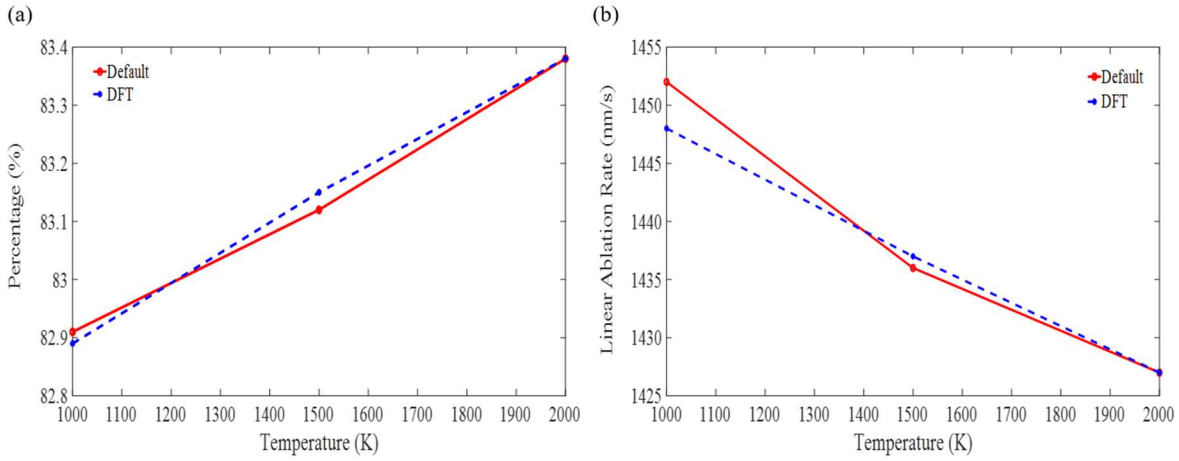

Figure 7. (a) ZrO_2/ZrC Percentage and (b) Linear Ablation Ratio of ZrO_2

Based on the basic physical properties, it was found that the density percentage of ZrO2 increases with increasing temperature. In this study, the physical parameters obtained through DFT calculations were used as input values for CFD.

Compared to the experimentally based physical property values built-in the program, it can be seen that the analysis results based on the DFT calculation results show a similar trend.

3.3. O2 dissociation

Figure 1 shows how oxygen molecules break apart on the (100) and (111) surfaces of ZrC and HfC, using graphs to display how the reaction unfolds over time and its energy dynamics. For ZrC on the (100) surface, the measurement of oxygen molecule separation starts with fluctuations around 1.5 Å, then jumps sharply, marking the point of dissociation (**Figure 1a**). The corresponding energy graph reveals a notable barrier of 0.03 eV that oxygen needs to overcome to dissociate is shown in **Figure 1b**. HfC exhibits a similar pattern, with oxygen separation stable at about 1.5 Å before it increases significantly, indicating the oxygen molecules breaking apart on

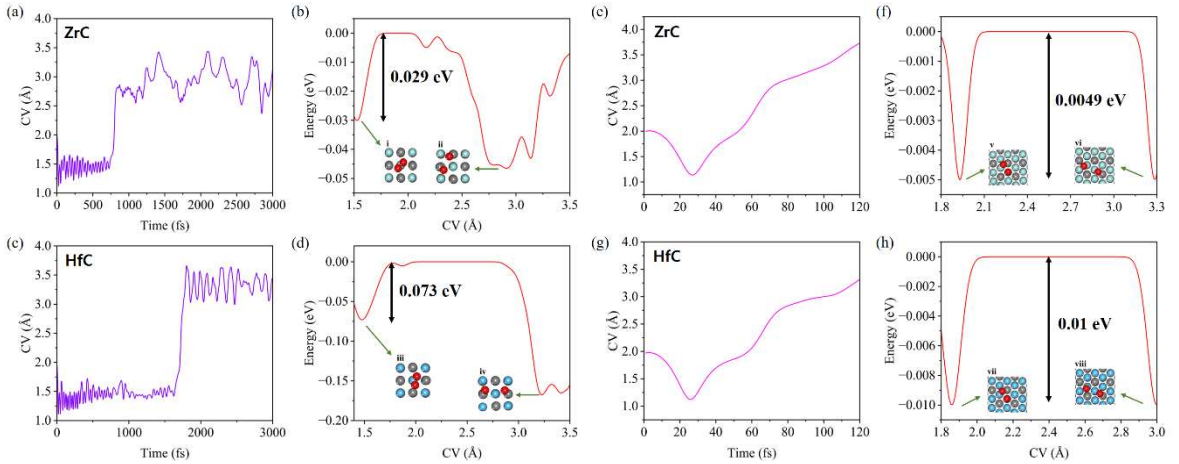

Figure 8. Evolution of collective variable (CV) and estimated free energy landscape of O2 dissociation

on (100) surface of ZrC (a - b), HfC (c - d) and (111) surface of ZrC (e - f), HfC (g - h). Insets shown in the figure describe the evolution of structural configuration of oxygen atoms on ZrC and HfC.

the surface (**Figure 1c**). However, a higher energy barrier of 0.075 eV (**Figure 1d**) for HfC suggests a stronger initial bond and a more significant energy requirement for dissociation compared to ZrC. The simulation further reveals that the dissociation process concludes within a remarkably brief timeframe of 3 ps, substantiating the efficiency of the chosen time step for the simulation. The energy barriers estimated for the dissociation on the (111) surface is substantially lower (0.005 eV for ZrC and 0.01 eV for HfC), indicating an enhanced reactivity. This finding corroborates the material's inherent resistance to oxidation, with HfC displaying a higher activation energy compared to ZrC on the (111) surface, consistent with its general oxidation resistance.

3.4. Surface Stability Analysis - Diffusion coefficient

The optimized MC configurations on both the (100) and (111) planes are shown in **Figure 8,** respectively. Following the optimization, a noticeable reduction in M-C bond lengths is seen on the (111) plane (see **Figure 1**). To evaluate surface stability before oxygen atom adsorption, the surface energy was computed using Equation 1, as detailed in the Supplementary Information (SI). The (100) plane demonstrates superior stability over the (111) plane, supporting previously reported studies. Further reinforcing these observations, diffusion coefficient values were calculated across various temperatures using AIMD simulation. These calculations reveal that the (100) surface consistently exhibits lower DC values across the temperature range studied than the (111) surface.

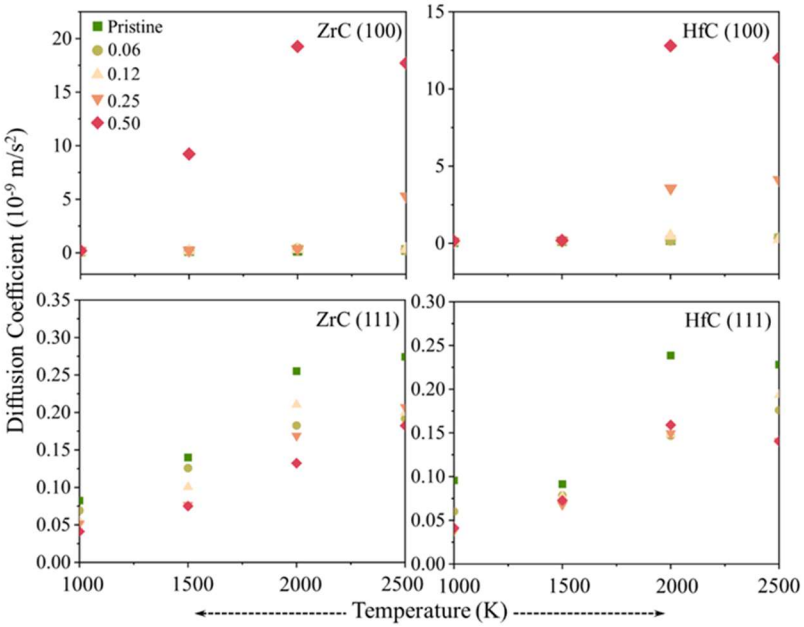

Figure 9. Temperature-dependent DC's of ZrC and HfC on (100) and (111) surfaces. DC's of pristine and doped ZrC and HfC surfaces at various temperatures, ranging from 1000 K to 2500 K. O coverage levels are represented by unique symbols and colors for clarity: pristine (green square), 0.06 (olive circle), 0.12 (yellow triangle), 0.25 (orange inverted triangle), and 0.50 (red diamond).

For oxygen coverage systems, data **Figure 8** from indicates that all plots demonstrate that the diffusion coefficient increases with temperature for both ZrC and HfC on (100) and (111) planes. This is an expected behaviour as higher temperatures typically increase atomic movement, resulting in higher diffusion rates. Pristine surfaces, without any oxygen coverage, typically have higher diffusion coefficients than the oxygen-covered surfaces, particularly at higher temperatures. This suggests that oxygen presence hampers the mobility of diffusing species, which could be due to the increased surface interaction or changes in the surface energy landscape. The DC's on the (100) planes are generally higher than those on the (111) planes for both ZrC and HfC. This suggests that the distribution of carbon atoms on the (100) surface of Zr-C markedly impacts its diffusion characteristics. The DC's for different O coverages show varying trends. In general, there is a noticeable effect of oxygen coverage

on the diffusion rate. For instance, in the case of ZrC and HfC (111), increased oxygen coverage seems to result in a decrease in the diffusion coefficient. This suggests that oxygen atoms may be acting as barriers to diffusion, possibly by creating stronger bonds with the surface atoms or by blocking diffusion pathways in the pure metal surfaces. At the highest O coverage of 0.50 ML, the DC's are the lowest among the oxygen coverages, particularly for ZrC and HfC on the (111) plane. This suggests a saturation effect (Zr-O film) where the presence of oxygen severely limits the movement of diffusing species, possibly due to a near-complete coverage that limits available diffusion sites. But in the (100) shows the highest DC values. When comparing the DC's between ZrC and HfC, it is evident that ZrC shows higher diffusion rates than HfC on the (100) and (100) surfaces, especially at higher temperatures. This could be attributed to the different material properties of ZrC and HfC, such as lattice parameters, bond strength, and surface reactivity. Hence, both oxygen coverage and temperature play significant roles in determining the diffusion rates on ZrC and HfC surfaces. Higher temperatures increase diffusion rates, whereas higher oxygen coverage decreases them in the (111) surfaces where the crystal orientation also plays a role, the (100) surface generally allowing higher diffusion rates than the (111) plane. The specific material differences between ZrC and HfC also contribute to the observed diffusion behaviour.

3.5. Oxygen adsorption

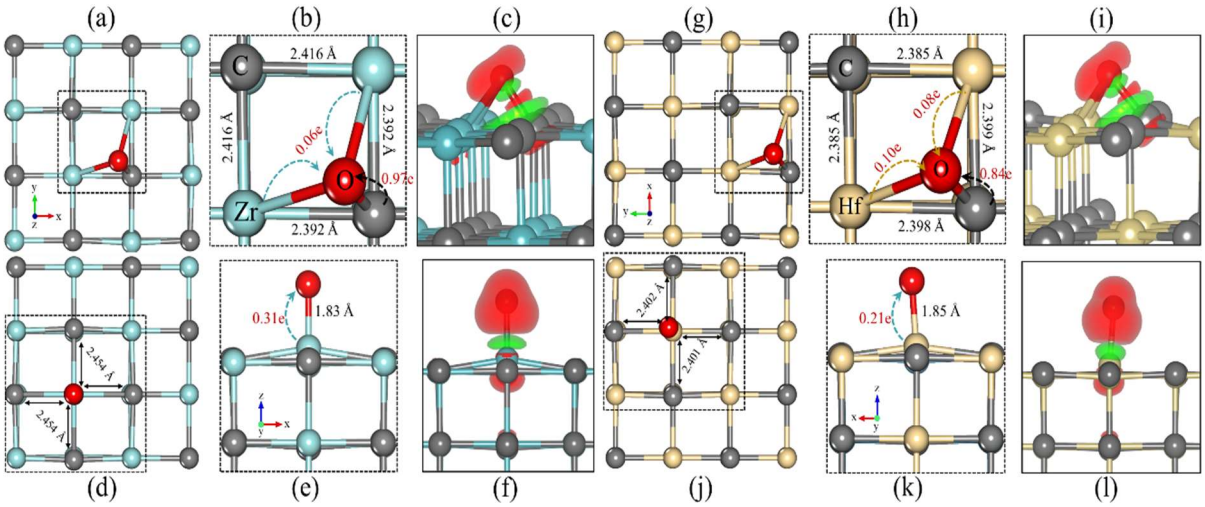

Figure 10. (a-f) Illustration of oxygen adsorption on C and Zr atoms at the surface (100) and (111). (a, d) adsorption (MMC) site (b, e) changes in bond length of Zr-C and charge transfer between O and ad atoms (c, f) side view of CDD during the adsorption process. (g-l) Illustration of oxygen adsorption on C and Hf atoms at the surface (100) and (111). (g,j) adsorption (MMC) site (h,k) changes in bond length of Hf-C and charge transfer between O and ad atoms (i,l) side view of CDD during the adsorption process.

Atomic oxygen can attach to various high-symmetry sites on the (100) and (111) surfaces of metal carbides, specifically atop a metal atom (M-top) and at the 3-fold hollow site composed of two metals and one carbon atom (MMC). Illustrations indicate that oxygen atoms are positioned nearer to the carbon atom in MMC sites, adopting an almost C-top configuration, with the oxygen atom forming an angle of 68° relative to the carbon atom and perpendicular to the surface and a C-O distance of 1.44 Å 11. The adsorption of single oxygen atoms on the (100) surface is significantly exothermic (ΔE = -3.29 eV), attributed to the strong interaction between the adsorbed oxygen atoms and the surface carbon atoms at the MMC site. Hence, the MMC site is the most favored on-surface adsorption site. Charge density difference (CDD) plots demonstrate the formation of a covalent bond when oxygen is adsorbed on the MMC sites 12. Furthermore, adsorption energies marginally increase as coverage expands, as the accompanying table details. When oxygen atoms are adsorbed on M-top sites, they influence only the metal atom, causing it to shift outward. The distances between M and oxygen atoms at M-top sites are higher (1.83 Å) than those at MMC sites, reflecting the weaker adsorption energy of -1.05 eV. Additionally, the charge transfer from O to Zr (0.3086e) is lower than from O to C (0.8835e), indicating a lesser extent of interaction. This is corroborated by the CDD analysis, which highlights the ionic nature of the bond between oxygen and zirconium. For the (111) surfaces, the adsorption of

oxygen atoms takes place preferentially at the hexagonal close-packed (HCP) sites. This specific adsorption configuration is found to be the most stable energetically, with adsorption energies of approximately –6.4 eV and –6.7 eV for ZrC and HfC (111) surfaces, respectively. These values indicate a strong affinity of oxygen for these surfaces, highlighting their significance in terms of stability and reactivity.

Table 3. Adsorption energy of oxygen atom on pristine and doped ZrC and HfC of (100) and (111) surfaces.

System	Single Oxygen atom Adsorption energy (*ΔE*) in eV/ Bond distance in Å on the surfaces		
	100		111
	C (MMC)	M (Zr or Hf) (M-top)	Zr
ZrC	-3.29/1.44	-1.05/1.83	-6.4[13]
HfC	-3.12/1.42	-0.84/1.85	-6.7

In the present study, the O adsorption at a higher coverage is also investigated. It is found that the MMC site in (100) and the HCP site in (111) are always the energetically preferred adsorption sites.

3.6. Oxygen Adsorption Impact on Zr-C Bond Length

Oxygen adsorption on the surface leads to a notable expansion in the bond length between zirconium and carbon atoms. As illustrated in **Figure 1**, upon the adsorption of oxygen onto carbon at the MCC site, there is a discernible increase in the Zr-C bond length from 2.392 Å to 2.416 Å. This elongation is attributed to the charge transfer from the oxygen atom to both zirconium and carbon atoms, resulting in an augmented charge density around these atoms. The repulsive forces exerted by the newly charged oxygen atom on adjacent carbon atoms contribute to the increased bond length between zirconium and carbon, serving as a precursor to the initial stages of surface distortion. Such distortion becomes more pronounced with the adsorption of more oxygen atoms, indicating a direct correlation between oxygen adsorption density and the extent of surface alteration.

3.7. Oxidation Mechanism-CO formation

The transformation of zirconium carbide (ZrC) to zirconium dioxide (ZrO2) involves oxygen replacing carbon in ZrC, leading to an intermediate phase that further reacts to form ZrO2 and carbon monoxide 14. This process, which includes the release of carbon atoms, is particularly challenging for certain ZrC surfaces due to a protective layer of Zr that hinders carbon removal. Unlike some reactions, carbon monoxide formation at low temperatures is not observed in this case. Further, oxygen once an overlayer is fully formed, and unlike the scenario with the O/ZrC (100) system, the formation of a CO does not occur at low temperatures. It is believed that the liberation of C atoms from the substrate is a critical step in the oxidation process of ZrC. This process is particularly challenging for ZrC (111) because its surface is shielded by a hexagonal layer of Zr, which hinders the removal of C atoms1.

Figure 10 depicts the oxidation behavior of the (100) and (111) surfaces of Zirconium Carbide (ZrC) and Hafnium Carbide (HfC) under high-temperature conditions (2500 K) with 0.25 ML oxygen coverage, as observed from Ab Initio Molecular Dynamics (AIMD) simulations. For the (100) ZrC surface, oxygen interaction initiates with simultaneous bonding to carbon and Zr atoms, prominently at the mmc site within 72 fs. By 120 fs, the interaction causes an upward displacement of carbon, and by 180 fs, dissociation occurs leading to carbon ablation from the surface and the formation of CO in the gas phase. At 337 fs, further oxygen adsorption is noted at the sites of carbon vacancy. An analogous sequence is observable on the (100) HfC surface, with initial oxygen adsorption at 158 fs, subsequent carbon movement at 184 fs, and CO formation with vacancy generation by 337 fs. In contrast, the (111) surface of both ZrC and HfC exhibits a different behavior. The oxygen atoms are adsorbed but do not result in the penetration of the surface or the formation of gaseous CO, even as the simulation advances. Instead, a stable oxide layer forms due to the strong bond between the oxygen and the metal atoms, attributable to the metallic atom-dominated surface which provides resistance to oxidation. This stability contrasts with the (100) surfaces, where the presence of surface carbon leads to more frequent

oxidative degradation. These observations underscore the facet-dependent oxidation mechanisms of ZrC and HfC and illustrate the significance of surface atomic composition in high-temperature oxidation processes.

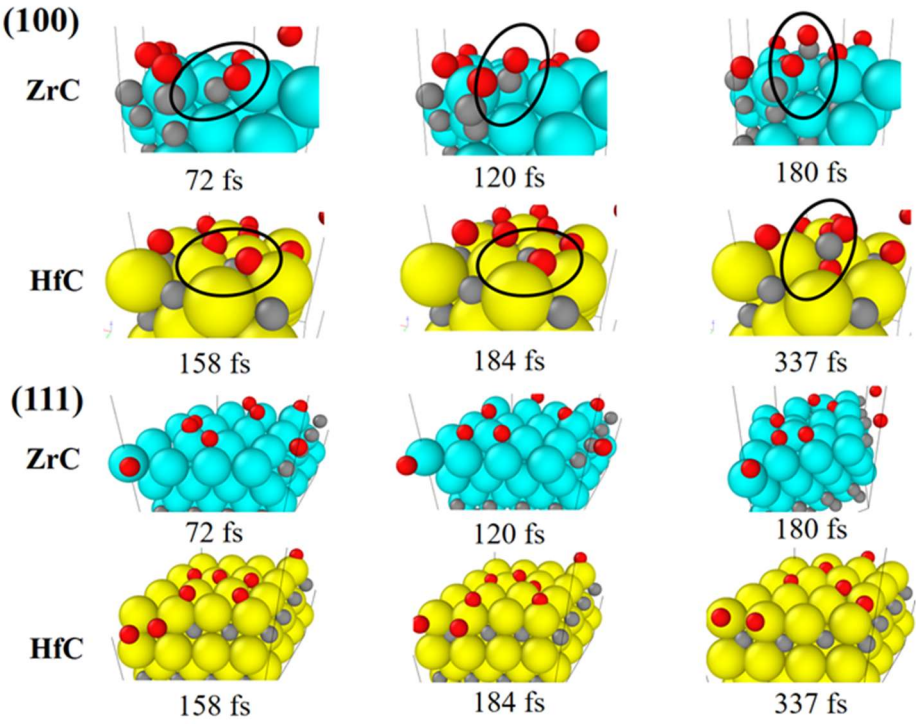

Figure 11. Snapshots of oxidation of ZrC and HfC from AIMD simulations at 2500 K with 0.25 ML surface oxygen coverage

4. Conclusion

we have established a Computational Fluid Dynamics (CFD) multiscale framework incorporating aerothermal and chemical aspects, using Density Functional Theory (DFT) analysis results. While there is known experimental data for UHTC ceramics, the thermal/mechanical properties and chemical reaction with atmospheric gas of newly developed heat shield materials need substantial time to acquire. However, by comparing DFT analysis results with experimental data, we have discovered the applicability of DFT-derived values in COMSOL Multiphysics CFD simulations. As a result, we constructed a CFD/DFT framework applicable to space reentry environment simulations and compared the oxidation performance of UHTCs.

After the oxidation performance understanding at continumm level **,**The nanoscale study provides a comprehensive analysis of O2 dissociation, surface stability, and diffusion behaviors of ZrC and HfC, uncovering the nuanced interplay between surface orientation, temperature, and oxygen coverage in determining their oxidation resistance. HfC has stronger oxygen bonds and requires more energy to break them, particularly on its (111) surfaces, which suggests it's better at resisting oxidation than ZrC. The (100) surfaces are more stable and less prone to diffusion, showing that carbon's arrangement on these surfaces plays a role. Temperature increases lead to more diffusion, but high oxygen levels can prevent this, particularly on the (111) surfaces. At maximum oxygen levels, diffusion is significantly reduced. Under high temperatures, ZrC and HfC behave differently: ZrC quickly oxidizes on its (100) surfaces, while HfC's (111) surfaces resist oxidation by forming a stable oxide layer. These findings highlight how a material's surface structure is crucial for its performance in extreme environments and can assist the design of materials that withstand high temperatures better.

Consequently, we have constructed a framework that can be employed for Earth re-entry environment simulations by obtaining thermal/mechanical properties and chemical reactions for newly developed heat shield materials and high-temperature ceramics.

Acknowledgement

This research was financially supported by the Institute of Civil Military Technology Cooperation funded by the Defense Acquisition Program Administration and Ministry of Trade, Industry and Energy of Korean government under grant No. 22-CM-19. Authors are grateful for the support.

References

1. Grossman, E. and I. Gouzman: Space environment effects on polymers in low earth orbit. Nuclear Instruments and Methods in Physics Research Section B: Beam Interactions with Materials and Atoms. 208, 48-57 (2003)
2. Jiang J. et al.: Temperature-dependent elastic and thermodynamic properties of ZrC, HfC, and their solid solutions (Zr0.5Hf0.5)C. Journal of the American Ceramic Society. 106(3), 2024-2036 (2023)
3. Ye, Z., Zhao, J., Zhu, B., Jing, Z., Sun, X., Stemmer, C., ... & Wen, D. (2023). A hybrid CFD-RMD multiscale coupling framework for interfacial heat and mass simulation under hyperthermal ablative conditions. *International Journal of Heat and Mass Transfer*, *213*, 124341.
4. Liu, G. et al.: Damage behavior of atomic oxygen on zirconium carbide coating modified carbon/carbon composite. Ceramics International. 46(3), 3324-3331 (2020)
5. Liu, Guangwei: Coupling of Gas-Surface Interaction and Material Response in Hypersonic Ablation. McGill University (2022)
6. Guillermet, F.: Analysis of thermochemical properties and phase stability in the zirconium-carbon system. Journal of Alloys and Compounds. 217(1), 69-89 (1995)
7. Lengauer, W. et al.: Solid state properties of group IVb carbonitrides. Journal of alloys and compounds. 217(1), 137-147 (1995)
8. Abdollahi, A.: First-principle calculations of thermodynamic properties of ZrC and ZrN at high pressures and high temperatures. Physica B: Condensed Matter. 410, 57-62 (2013)
9. Lawson, C. et al.: Thermal expansion and atomic vibrations of zirconium carbide to 1600 K. Philosophical Magazine. 87(17), 2507-2519 (2007)
10. Grossman, N.: High-temperature thermophysical properties of zirconium carbide. Journal of the American Ceramic Society. 48(5), 236-242 (1965)
11. H. Fu, W. Peng and T. Gao, *Mater Chem Phys*, 2009, **115**, 789–794.
12. W. Weber, *Lattice Dynamics of Transition-Metal Carbides Volume 8*, 1973, vol. 8.
13. X. Tao, H. Chen, Y. Zhou, Q. Peng and Y. Ouyang, *Journal of Nuclear Materials*, , DOI:10.1016/j.jnucmat.2021.153235.
14. A. M. Nartowski, I. P. Parkin, M. Mackenzie, A. J. Cravenb and I. Macleodb, *Solid state metathesis routes to transition metal carbides, volume-9*, 1988.
15. Z. Wu, X. J. Chen, V. V. Struzhkin and R. E. Cohen, *Phys Rev B Condens Matter Mater Phys*, , DOI:10.1103/PhysRevB.71.214103.
16. K. Nakamura and M. Yashima, *Materials Science and Engineering: B*, 2008, **148**, 69–72.
17. W. Sun, X. Kuang, H. Liang, X. Xia, Z. Zhang, C. Lu and A. Hermann, *Physical Chemistry Chemical Physics*, 2020, **22**, 5018–5023.
18. Jiang, J., Shi, Z., Arramel, Zhang, J., Deng, T., & Li, N. (2023). Temperature-dependent elastic and thermodynamic properties of ZrC, HfC, and their solid solutions (Zr0. 5Hf0. 5) C. *Journal of the American Ceramic Society*, *106*(3), 2024-2036.
19. Lawson, A. C., Butt, D. P., Richardson, J. W., & Li, J. (2007). Thermal expansion and atomic vibrations of zirconium carbide to 1600 K. *Philosophical Magazine*, *87*(17), 2507-2519.

20. Guillermet, A. F. (1995). Analysis of thermochemical properties and phase stability in the zirconium-carbon system. *Journal of Alloys and Compounds*, *217*(1), 69-89.